



# An AI Based Algorithm for Retrieving Aerosol Optical Depth and Single Scattering Albedo Using All-Sky Imager Observations

Heyang Ni<sup>1</sup>, Jing Li<sup>\*,1,2,3</sup>, Liang Chang<sup>1</sup>, Yueming Dong<sup>1</sup>, Guanghao Du<sup>1</sup>, Muqian Li<sup>1</sup>, Qiurui Li<sup>1</sup>, Guanyu Liu<sup>1</sup>, Yuebo Sun<sup>1</sup>, Angnuo Tian<sup>1</sup>, Sheng Yue<sup>1</sup>, Chongzhao Zhang<sup>1</sup>, Zhenyu Zhang<sup>1</sup>

5 <sup>1</sup>Department of Atmospheric and Oceanic Sciences, School of Physics, Peking University, Beijing, China

<sup>2</sup>Institute of Carbon Neutrality, Peking University, Beijing, China

<sup>3</sup>Center for Environment and Health, Peking University, Beijing, China

Correspondence to: jing-li@pku.edu.cn

**Abstract.** Accurate measurement of aerosol optical properties is critical for understanding their radiative and environmental  
10 impacts. Currently, the most accurate retrieval of aerosol properties comes from the multi-channel surface sun photometer, but  
with relatively high cost and deployment/maintenance requirements. Here we develop a novel AI based method for retrieving  
daytime aerosol optical parameters, namely aerosol optical depth (AOD) and single scattering albedo (SSA) using images  
acquired by All-Sky Imagers (ASI). Surface based AOD and SSA retrievals from surface sun photometers are used as the  
training targets. Algorithm training and retrievals were performed for two sites in East China and Central US respectively.  
15 Independent validation against ground-based measurements demonstrated high consistency between the ASI-retrieved and sun  
photometer measured AOD and SSA, with Pearson correlation coefficients ( $r$ ) exceeding 0.86 for AOD across all wavelengths  
at both sites and Root Mean Square Errors (RMSE) below 0.25. For SSA,  $r$  values reached 0.67 at the Beijing\_PKU site and  
0.84 at the SGP site, with RMSE remaining below 0.09 across all spectral channels, demonstrating the feasibility of  
simultaneous AOD and SSA retrieval from low-cost all-sky imagers. This method not only overcomes the high computational  
20 cost associated with traditional radiative transfer iterative algorithms, but also provides great potential for denser surface  
aerosol measurements by leveraging the low-cost and easy-maintenance advantages of the all-sky imager.

## 1 Introduction

Aerosol radiative forcing remains a major source of uncertainty in climate assessment due to its high spatiotemporal  
heterogeneity and complex composition (Bellouin et al., 2020; Boucher et al., 2013; Intergovernmental Panel On Climate  
25 Change (Ipc), 2023; Li et al., 2017). Mitigating this requires accurate retrieval of optical properties, particularly Aerosol  
Optical Depth (AOD) and Single Scattering Albedo (SSA) (Hansen et al., 1997; Hao et al., 2024; Levy et al., 2013). While  
ground-based sun photometers, such as those used within the Aerosol Robotic Network (AERONET) can provide the most  
accurate retrievals of aerosol properties (Holben et al., 1998), the relatively high cost of the instrument limits their extensive  
spatial deployments.



30 Traditional aerosol monitoring networks, such as AERONET, provide high accuracy but are limited by high equipment costs  
and sparse spatial coverage. To address this, various low-cost retrieval methods have been developed (Kazantzidis et al., 2017;  
Snik et al., 2014). These include retrieving AOD from long-term visibility records (Hao et al., 2024), employing all-sky imaging  
systems combined with machine learning (Scarlatti et al., 2023), and utilizing portable handheld sun-photometers like  
Calitoo (García et al., 2025). Among them, the all-sky imager (ASI), originally designed for automated ground-based cloud  
35 cover monitoring to replace manual observations, has emerged as a powerful tool for environmental research (Sabburg and  
Wong, 1999). Typically equipped with a fisheye lens and Charge-Coupled Device (CCD) sensors, these cameras capture high  
spatial-and-temporal-resolution visible-light images across the entire sky dome. Recent advancements in quality and  
calibration have rendered ASIs highly suitable for atmospheric measurement (Ghoniya et al., 2012; Kazantzidis et al., 2012,  
2017; Tohsing et al., 2013; Valdelomar et al., 2021). Numerous studies have demonstrated the potential of All-Sky Imagers  
40 (ASIs) for retrieving aerosol optical properties. Early approaches primarily relied on Radiative Transfer Models (RTM) and  
Look-Up Tables (LUTs) to link sky radiance or the Red-to-Blue Ratio (RBR) to AOD (Huo and Lü, 2010; Olmo et al., 2008).  
With the advent of data-driven techniques, Machine Learning (ML) and Deep Learning models have been increasingly applied,  
utilizing pixel-level features and circumsolar information to bypass complex physical calibrations (Logothetis et al., 2023b;  
Scarlatti et al., 2023).

45 Compared to traditional sun photometers, ASIs offer three significant advantages: lower equipment and maintenance costs;  
enhanced spatial coverage, particularly in remote areas like deserts or solar power plants where stations are sparse (Kazantzidis  
et al., 2017); and the avoidance of temporal delays, as ASIs capture radiance from multiple sky locations simultaneously rather  
than sequentially (Román et al., 2022). However, quantitative inversion of aerosol properties from ASI data faces significant  
challenges. Historically, ASI-based aerosol retrievals have predominantly relied on extracting sky radiances or RGB channel  
50 intensities and mapping them to Aerosol Optical Depth (AOD, (Rossini and Krenzing, 2007; Tohsing et al., 2013). These  
inversions are typically driven either by establishing a lookup table (LUT) between the radiation ratio (blue/red light) and  
AOD (Huo and Lü, 2010), or by employing data-driven machine learning algorithms (Cazorla et al., 2009; Logothetis et al.,  
2023c; Scarlatti et al., 2023). While these pioneering studies have demonstrated reasonable AOD estimation accuracy—often  
achieving Root Mean Square Errors (RMSE) of less than 0.1 when validated against standard AERONET measurements under  
55 clear-sky conditions (Logothetis et al., 2023c, a; Scarlatti et al., 2023)—their practical applications remain restricted. Most of  
these works are confined to single-station validations, leaving their multi-station scalability and robustness under varying  
surface albedos largely untested.

Furthermore, traditional inversion approaches are computationally complex and inefficient, typically involving resource-  
intensive iterative adjustments of inputs into RTMs (Olmo et al., 2008). Crucially, most existing ASI-based studies focus solely  
60 on AOD inversion. They fail to achieve the simultaneous retrieval of aerosol scattering properties, hindering an integrated  
analysis of aerosol mass and particle composition at fine scales.

The visible-band imagery captured by ASIs not only contains direct attenuation of solar radiation that is essential to derive  
AOD, but also captures characteristics of diffuse radiation, which is typically measured by sun photometers to retrieve



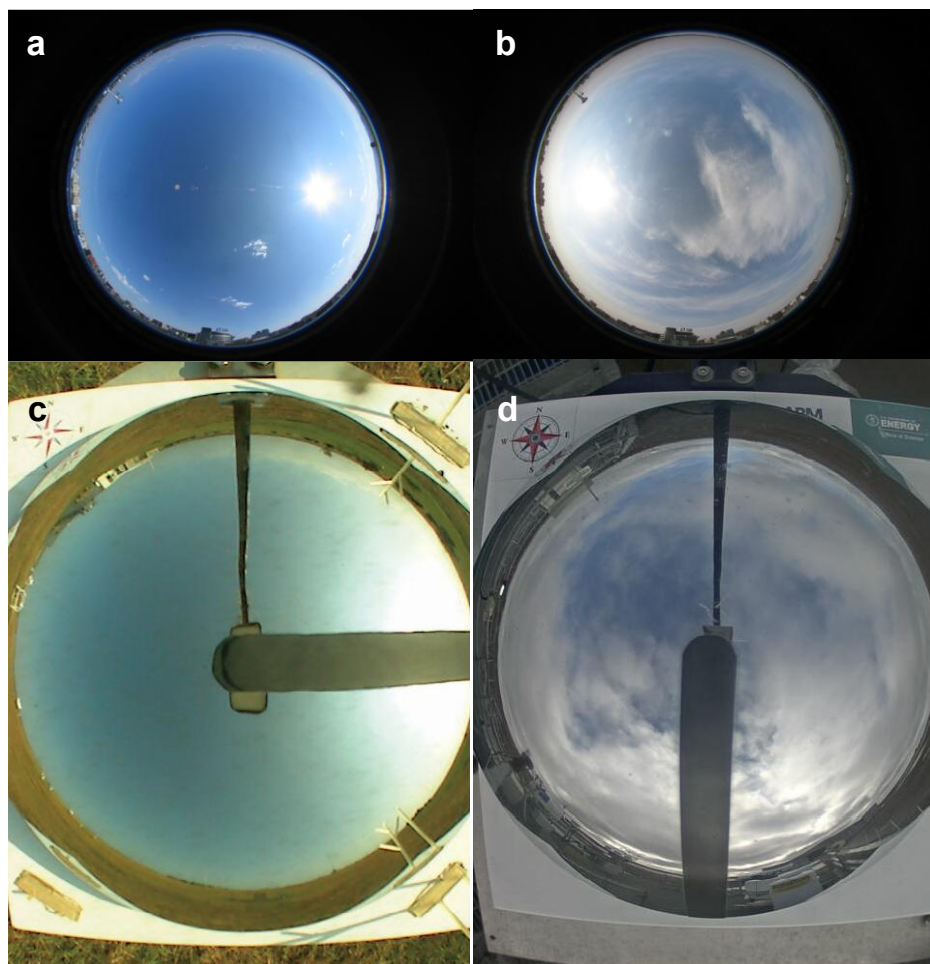
SSA(Dubovik and King, 2000). However, this feature is not fully utilized by previous aerosol retrieval practices with ASI. To  
65 address this gap, this study proposes a scheme to simultaneously retrieve AOD and SSA from ASI images. By constructing  
machine learning regression models, such as eXtreme Gradient Boosting (XGBoost, (Chen and Guestrin, 2016), we leverage  
the capability of these algorithms to uncover patterns within the data. This approach also greatly simplifies the complex  
iterative process of traditional inversion to enhance efficiency. Our algorithm provides a pathway for extensive low-cost  
aerosol observations, thus providing practical value for reducing aerosol-related uncertainties in climate assessments.

## 70 **2. Data and Method**

### **2.1 All-Sky Imager Data**

The data used in this study were collected at two sites: Beijing in north China and the Southern Great Plain (SGP) site in central  
US. The ASI data in Beijing were collected by an SRF-02 All-Sky Imager manufactured by EKO. This imager lacks a solar  
occluding device, and its external appearance and sample images are shown in Fig. 1a-c. The all-sky imager was installed at  
75 the School of Physics, Peking University (39°59'N, 116°18'E). Images were captured between April 2017 and January 2020,  
with a resolution of  $2272 \times 1704$  pixels at 180 dpi, totaling approximately 200,000 images.

The SGP site (shown in Fig. 1d-f), operated by the U.S. Department of Energy's Atmospheric Radiation Measurement (ARM)  
program, serves as a key atmospheric observation station(Cook and Sullivan, 2025; Stokes and Schwartz, 1994). Sky  
conditions were monitored using the Total Sky Imager (TSI), Model TSI-660, developed by Yankee Environmental Systems  
80 (YES), Inc. To evaluate the model's performance under different climatic conditions and geographical contexts, data spanning  
from January 2024 to November 2024 were selected from the SGP site. This period is distinct from the Beijing dataset (2018–  
2020), providing an opportunity to assess the method's transferability and robustness across different environments.



85 **Figure 1:** (a) A sample image captured by Beijing\_PKU site ASI; (b) A sample cloud image captured by Beijing site ASI; (c) A sample image captured by SGP site ASI; (d) A sample cloud image captured by SGP site ASI. Source for (c, d): ARM user facility ([https://adc.arm.gov/discovery/results/instrument\\_class\\_code::tsi](https://adc.arm.gov/discovery/results/instrument_class_code::tsi)), licensed under CC BY 4.0 (<https://creativecommons.org/licenses/by/4.0/>). Last access: 21 April 2026.

## 2.2 Sun Photometer Data

The target AOD and SSA are obtained from collocated surface sun photometers, namely those at the ‘Beijing\_PKU’ and  
90 ‘ARM\_SGP’ sites of AERONET. AOD from direct measurements and SSA retrieved from diffuse sky measurements at four  
wavelengths (440, 675, 870, and 1020 nm) are used. The dataset covers the period from 2017 to 2021 for Beijing\_PKU and  
from 2024 to 2025 for SGP. For the SGP site, we utilized the Version 3 Level 2.0 (cloud-screened and quality-assured) data  
products for both AOD and SSA. This dataset represents the highest quality standard of AERONET, providing a robust  
benchmark for model validation in cleaner atmospheric environments. For the Beijing site, we adopted a different strategy to  
95 balance data quality and sample availability. While Level 2.0 data are preferred, the strict quality control criteria for SSA



inversion significantly reduce the number of valid retrievals, hindering the analysis of diverse pollution conditions. Therefore, we utilized Version 3 Level 1.5 (cloud-screened) products for Beijing.

### 2.3 AI Based ASI Aerosol Retrieval Algorithm

The inversion algorithm developed in this study comprises four main components: clean-sky image processing, image feature extraction, data matching, and the machine learning model. The overall technical framework of the proposed ASI-based aerosol retrieval algorithm is illustrated in Figure 2.

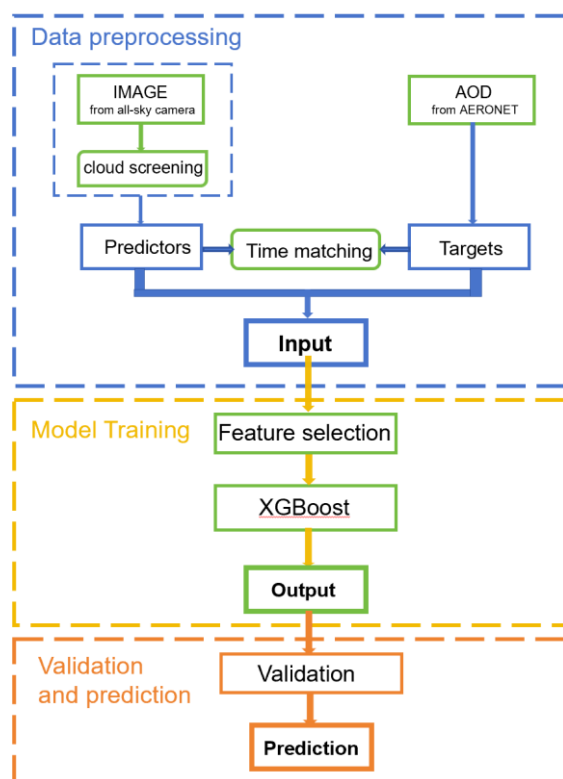


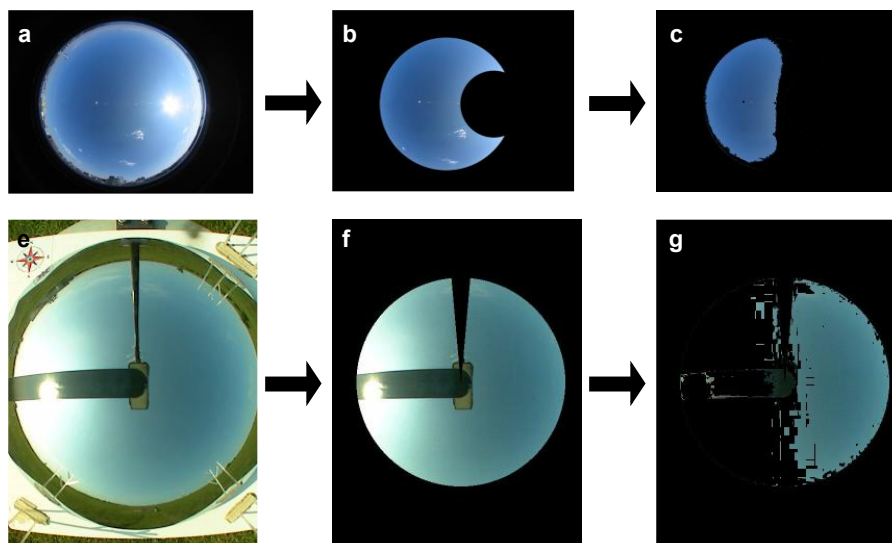
**Figure 2: Schematic flowchart of the proposed aerosol retrieval framework.**

Clean-Sky Image Processing: Upon acquiring time-stamped raw sky images, we first mask areas that interfere with the extraction of cloud-free sky radiance—namely buildings, clouds, and glare spots caused by the sun and lens artifacts. The specific steps are:

- (a) Masking buildings at the image periphery.
- (b) Identifying and masking the brightest circular region (sun and its immediate surroundings).
- (c) Cloud and lens flare masking: Iterative threshold segmentation is applied until the threshold stabilizes, after which a



110 black mask is used to occlude high-brightness regions associated with clouds and flares(Anon, 1978; Gonzalez and Faisal, 2019; Zhang and Xiao, 2014).



115 **Figure 3: Visualization of the stepwise image processing workflow. The upper panels (a–c) and lower panels (d–f) display representative examples from the Beijing and SGP sites, respectively. From left to right: (a, d) the original raw full-color images; (b, e) the intermediate results after applying geometrical correction and solar disk masking; and (c, f) the final preprocessed images, with non-sky elements removed, ready for aerosol optical property retrieval. Source for (e): ARM user facility ([https://adc.arm.gov/discovery/results/instrument\\_class\\_code::tsi](https://adc.arm.gov/discovery/results/instrument_class_code::tsi)), licensed under CC BY 4.0 (<https://creativecommons.org/licenses/by/4.0/>). Last access: 21 April 2026.**

While the core retrieval algorithm remains consistent across both sites, a site-specific preprocessing step was implemented for  
 120 the SGP dataset to account for instrument differences. Unlike the setup at the Beijing site, the Total Sky Imager (TSI) at the SGP site is equipped with a sun occultation system (a sun-blocking strip and support arm) to prevent sensor saturation. This physical structure introduces permanent non-sky artifacts into the field of view. To address this, we applied a fixed fan-shaped digital mask to the SGP raw images prior to cloud screening and feature extraction. This mask effectively assigns zero weights to the pixels occupied by the occultation arm, excluding them from subsequent calculations. Beyond this geometric masking,  
 125 the entire downstream processing pipeline—including the extraction of statistical features (mean, standard deviation, and texture) and the XGBoost model architecture—remains identical to that applied at the Beijing site, ensuring methodological consistency.

Image Feature Extraction: We extract all colored pixels from the processed sky region image. Each pixel is represented by its Red (R), Green (G), and Blue (B) channel values. The mean values of R, G, and B across all these pixels are computed, and  
 130 the Red-to-Blue Ratio (RBR) is calculated as the ratio of the R mean to the B mean(Long et al., 2006). Using the image timestamp and geolocation, the solar zenith angle (SZA) is computed. Including SZA is crucial as it explicitly informs the model of the observation geometry, allowing it to decouple the geometrical dependence of sky radiance from aerosol-induced variations. To emulate the sun photometer’s Almucantar scanning mode (fixed zenith angle, varying azimuth), a circular annulus with a radius between 0.6 and 0.8 times the sky image radius is defined, centered on the image midpoint. At least 10



135 pixels are evenly sampled along this annulus to extract their specific RGB values, thereby capturing directional aerosol scattering information. Consequently, the final input feature vector constructed for the XGBoost model comprises the global RGB channel means, the RBR, the SZA, and the discrete RGB values obtained from the annulus sampling points.

Data Matching: Features extracted from the ASI are matched with aerosol optical parameters from the collocated AERONET instruments based on timestamps. A successful match requires the time difference between the AERONET measurement and  
140 the ASI image capture to be less than 5 minutes to ensure temporal consistency.

Machine Learning Algorithm: We developed a machine learning inversion method based on the XGBoost model, where model fitting was performed to establish a nonlinear mapping between the input features (observational data) and the target parameters to be inverted (Lary et al., 2016). The Root Mean Square Error (RMSE) was adopted as the loss function to quantify the fitting error and guide the optimization of the model. The optimal number of boosting iterations (N) was determined via 10-fold  
145 cross-validation with early stopping (Chai and Draxler, 2014). Using this optimal N and hyperparameters including a maximum tree depth of 7, learning rate of 0.08, subsampling ratio of 0.75, column sampling ratio of 1.0, and minimum loss reduction for leaf node splitting set to 0, the data was used to train the ensemble regression model. To ensure strictly independent validation and assess temporal generalization, the dataset was sorted chronologically. We utilized a time-series splitting strategy where the first two-thirds of data from each month formed the training set, and the subsequent one-third was reserved as the  
150 independent test set (Arlot and Celisse, 2009; Roberts et al., 2017). This approach prevents data leakage caused by the high temporal autocorrelation of atmospheric parameters (Karpatne et al., 2017). This strategy also ensures that the model is evaluated on unseen data while maintaining comprehensive seasonal coverage in both subsets. Following the chronological splitting strategy, the final experimental dataset for the four spectral channels was divided as follows: for the Beijing site, the training and independent test sets comprised 3675 and 2206 samples, respectively; for the SGP site, 1669 samples were used  
155 for training and 807 for testing.

This process yielded a model capable of joint output (e.g., SSA at 440 nm, AOD at 440 nm). The trained model was applied to the independent test set to generate predictions. Scatter density plots were constructed with AERONET values on the x-axis and predicted values on the y-axis. Gaussian kernel density estimation was used to visualize point density. A 1:1 reference line ( $y=x$ ) and a linear regression fit line ( $y = ax + b$ ) were overlaid. The proportionality was quantitatively assessed using the  
160 regression slope (k). This procedure was repeated for each of the four wavelength channels (440, 675, 870, 1020 nm), resulting in a trained ensemble regression model for each channel.

### 3. Results and Discussion

#### 3.1 Overall AOD and SSA retrieval performance by ASI

This section discusses the performance of the model at both the Beijing and SGP sites, evaluating its robustness and reliability  
165 across different climatic conditions.

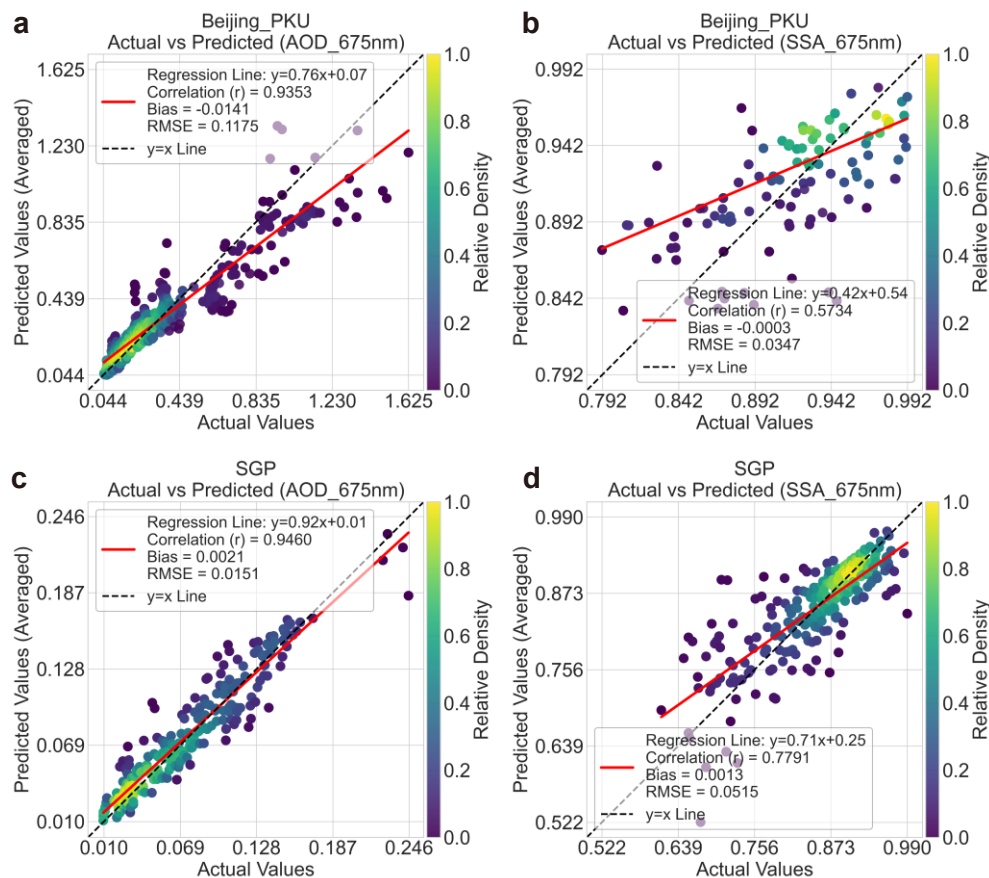


**Figure 4: Independent validation results of XGBoost model predictions at 675 nm for the Beijing\_PKU site (a, b) and the SGP site (c, d). Scatter plots show averaged predicted values versus actual values for AOD (a, c) and SSA (b, d). The red line represents the linear regression fit, and the black dashed line indicates the 1:1 reference line. Point colors indicate the relative density of observations. Statistical metrics including the Pearson correlation coefficient ( $r$ ), bias, and root mean square error (RMSE) are shown in each panel.**

170

Figure 4 displays the scatter density plots of AOD and SSA retrieved by the algorithm versus AERONET observations at 675nm for the Beijing and SGP sites over the entire study period.

**Table 1: Statistical summary of retrieval performance, including Pearson Correlation Coefficient ( $r$ ), Root Mean Square Errors (RMSE), and Mean Absolute Errors (MAE) for AOD and SSA across four spectral channels (440, 675, 870, and 1020 nm). Results are presented for (a, b) the Beijing site and (c, d) the SGP site.**

175



Site	Parameter	Metric	440nm	675nm	870nm	1020nm
Beijing	AOD	$r$	0.91	0.89	0.88	0.86
		$RMSE$	0.25	0.17	0.12	0.10
		$MAE$	0.15	0.09	0.06	0.06
	SSA	$r$	0.67	0.61	0.49	0.33
		$RMSE$	0.03	0.03	0.04	0.04
		$MAE$	0.03	0.02	0.03	0.04
SGP	AOD	$r$	0.89	0.91	0.92	0.87
		$RMSE$	0.05	0.03	0.02	0.02
		$MAE$	0.03	0.01	0.01	0.01
	SSA	$r$	0.64	0.79	0.83	0.84
		$RMSE$	0.08	0.06	0.07	0.09
		$MAE$	0.04	0.04	0.05	0.06

The retrieved AOD agrees well with AERONET AOD, with all data points closely distributed around the 1:1 line. For both sites, the Pearson correlation coefficient ( $r$ ) for AOD exceeds 0.86 across all wavelengths, demonstrating robust retrieval performance. The retrieval performance for SSA is lower compared to that of AOD, which is not surprising since SSA is highly sensitive to uncertainties in the diffuse measurements (Dubovik et al., 2000).

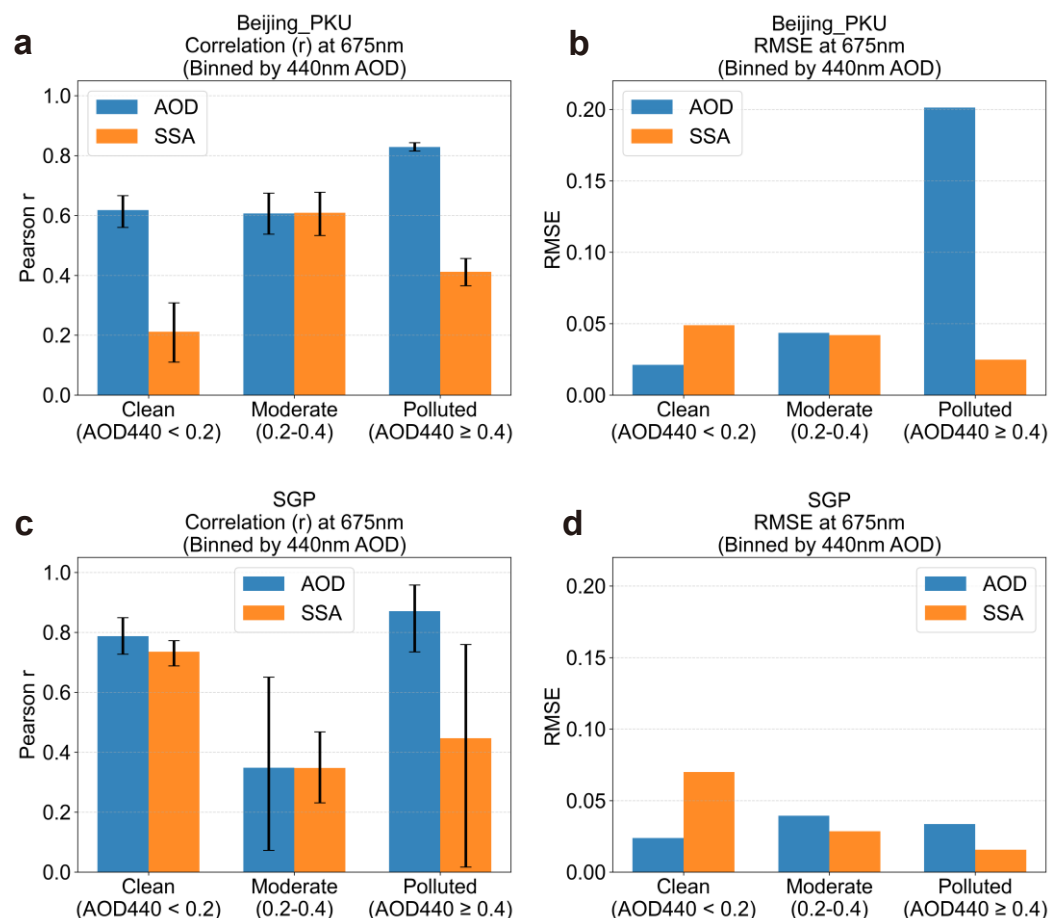
For the Beijing site, the model demonstrated robust performance in retrieving AOD across all wavelengths, with  $r$  values ranging from 0.86 to 0.91 and RMSE values of 0.10–0.25. SSA retrieval at Beijing showed moderate but wavelength-dependent performance: the correlation was highest at 440 nm ( $r = 0.67$ ) and decreased progressively toward longer wavelengths, reaching  $r = 0.33$  at 1020 nm. Despite the low correlation, RMSE remained consistently low ( $\leq 0.04$ ) across all bands, which may partly be attributed to the narrow dynamic range of SSA values at this site (Legates and McCabe Jr., 1999). For the SGP site, the model achieved higher overall accuracy than at Beijing. AOD retrieval yielded  $r$  values of 0.87–0.92 with notably low RMSE (0.02–0.05), reflecting the more stable aerosol conditions at this site. SSA retrieval also showed improved performance compared to Beijing, with  $r$  increasing from 0.64 at 440 nm to 0.84 at 1020 nm and RMSE remaining below 0.09. These evaluation metrics indicate that the algorithm can effectively retrieve AOD and SSA with reasonable accuracy and stability throughout the observation period.

### 3.2 Model Performance Under Different Aerosol Loadings

The accuracy of aerosol retrieval is typically associated with aerosol loading. To evaluate the performance of the algorithm more rigorously, we categorized the validation dataset into three regimes based on the reference 440 nm AOD: clean ( $AOD_{440nm} < 0.2$ ), moderate ( $0.2 < AOD_{440nm} < 0.4$ ), and polluted ( $AOD_{440nm} > 0.4$ ). Figure 5 illustrates the retrieval performance for 675



195 nm AOD and SSA across these regimes for both the Beijing and SGP sites. Note that the y-axis scales are unified to facilitate direct comparison.



200

**Figure 5: Retrieval performance of AOD and SSA at 675 nm under different aerosol loading regimes for the Beijing\_PKU site (a, b) and the SGP site (c, d). The data are binned based on the reference AERONET AOD at 440 nm: Clean (< 0.2), Moderate (0.2-0.4), and Polluted ( $\geq 0.4$ ). The left panels (a, c) display the Pearson correlation coefficient ( $r$ ) with error bars representing the 95% confidence intervals derived from bootstrap resampling ( $N=500$ ). The right panels display the Root Mean Square Error (RMSE).**

205

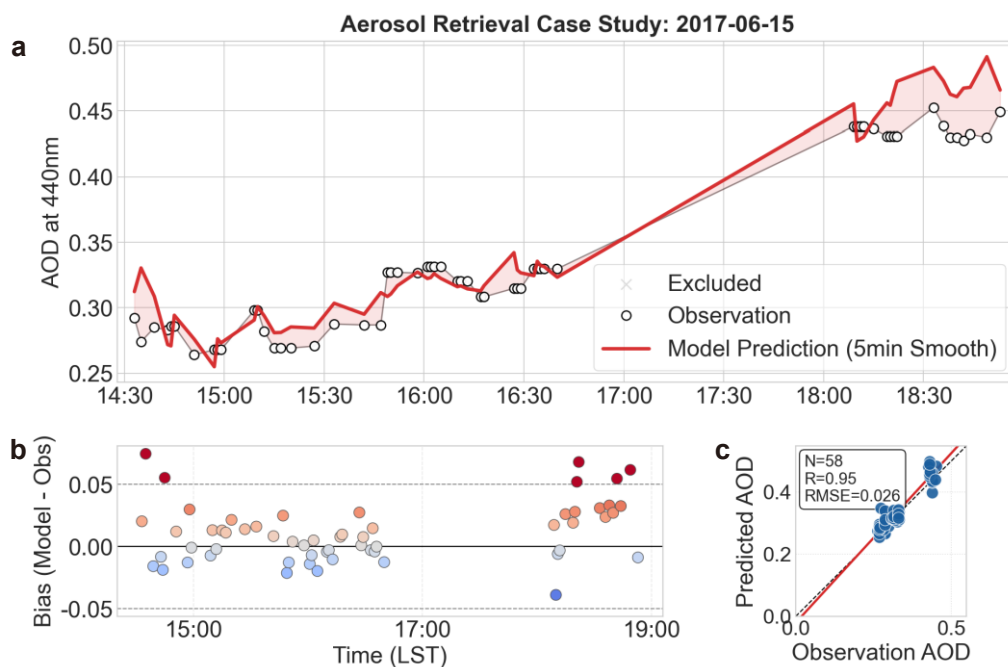
At the Beijing site (Fig. 5a-b), the AOD retrieval error exhibits a clear dependence on aerosol loading. In the clean and moderate regimes, the RMSE for AOD remains low ( $< 0.05$ ). However, in the polluted regime, the RMSE increases significantly to  $\sim 0.20$ . This reflects the challenge of retrieving extremely high aerosol loads in complex urban environments using ASI, where the signal saturation effect may degrade its sensitivity to aerosol loading. Regarding SSA, the correlation ( $r$ ) is notably low in the clean regime ( $r = 0.21$ ), which can be attributed to the extremely narrow dynamic range of SSA values under clean conditions, limiting the model's ability to capture variability. However, the RMSE for SSA remains reasonable ( $< 0.05$ ) across all regimes, confirming that the model correctly estimates the magnitude of absorption even when pixel-level correlation is limited by noise.



210 The SGP site (Fig. 5c-d) demonstrates superior stability. A striking contrast is observed in the polluted regime: while the AOD  
 RMSE at Beijing surges to 0.20 when  $AOD > 0.4$ , the RMSE of AOD at the SGP site remains remarkably low at  $\sim 0.035$ . This  
 is likely related to the fact that the "polluted" conditions at SGP are still optically thinner and less complex than the haze events  
 in Beijing that do not cause image saturation, thus allowing for more accurate retrievals. It should be noted that the relatively  
 low  $r$  values observed in the moderate regime for SGP (AOD:  $r = 0.34$ , SSA:  $r = 0.35$ ) may partly reflect a range restriction  
 215 effect, as the sample size in this bin is limited ( $N = 15$  in the test set), which can reduce statistical reliability (Jenkins and  
 Quintana-Ascencio, 2020). Despite this, the consistently low RMSE ( $< 0.05$  for AOD and  $< 0.08$  for SSA) across all bins  
 confirms the applicability of ASI in retrieving aerosol properties under cleaner atmospheric background of the Central US.

### 3.3 Evaluation of Diurnal Variability

220 A major advantage of ASI is the capability to retrieve aerosol properties with high temporal resolution, thus allowing for the  
 representation of aerosol diurnal cycle. Here we first selected June 15, 2017 at Beijing site as a representative case since AOD  
 on this day exhibited significant intra-day variation, providing an ideal condition for testing the model performance.



225 **Figure 6: Case study of diurnal AOD variation retrieval at the Beijing site on June 15, 2017. The top panel (a) compares the AERONET observations (black circles) with the model predictions that have not been independently validated (red solid line, smoothed using a 5-minute time window). The bottom panels display the time series of retrieval bias (b) and the scatter plot between observed and predicted AOD (c).**

As shown in the time series (Fig. 6a), the ASI retrieved AOD demonstrates remarkable consistency with ground-based AERONET observations. Note that a 5-minute time window smoothing technique was applied to the ASI AOD curve (red line) to filter out high-frequency retrieval noise. However, all statistical metrics reported in this study were calculated using the

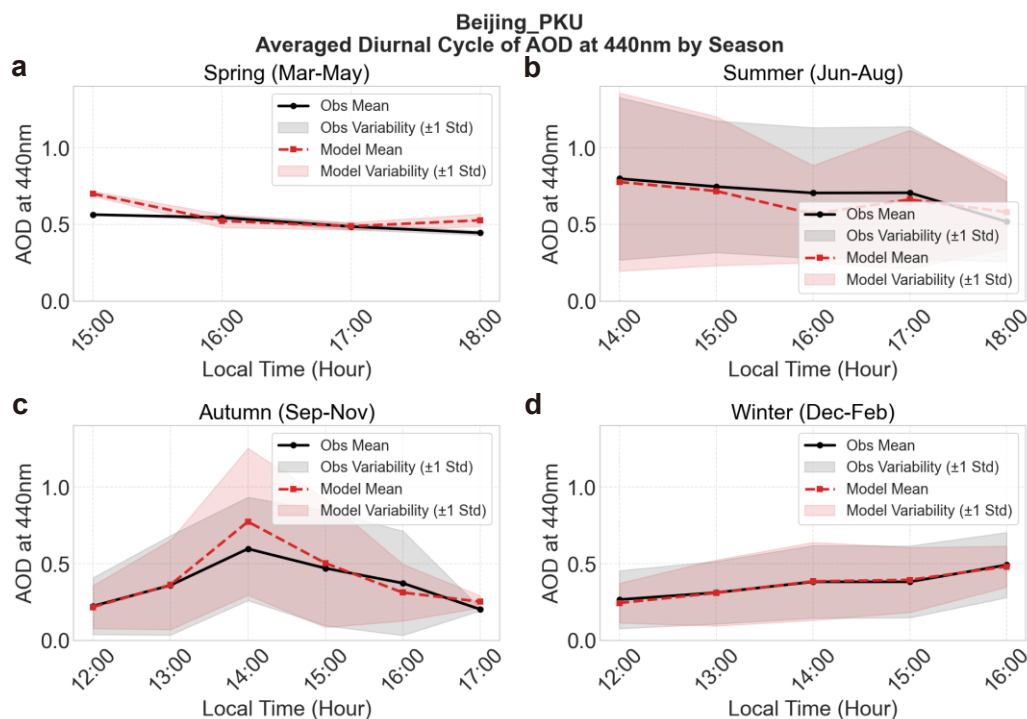


230 original, unsmoothed retrieval results to ensure rigorous validation. The ASI retrievals accurately capture the trend of AOD  
diurnal variability. AOD gradually increased and fluctuated from 15:00 to 18:00, and then stabilized, which is well captured  
by the ASI. While the observations showed a "stepped" pattern due to instrument sampling characteristics, the model retrieval  
(solid red line) successfully fitted the central tendency of these discrete points. Moreover, the model responds sensitively to  
rapid changes, demonstrating its sensitivity to short-term high-frequency variations in atmospheric aerosols.

235 The statistical metrics (Fig. 6c) further confirm the retrieval accuracy. With 58 sample points, the correlation coefficient ( $R$ )  
reached 0.95, and the Root Mean Square Error (RMSE) was only 0.026.  
The bias analysis (Fig. 6b) shows that the deviations for most data points were confined within  $\pm 0.025$ . Although minor  
overestimation occurred in the low-value period around 14:30 and 18:30, the overall bias distribution remained balanced  
without significant systematic errors.

240 It is worth noting that a similar high-frequency diurnal analysis was not performed for SSA. Unlike AOD, which is derived  
from high-frequency direct sun measurements, SSA is retrieved from the much less frequent almucantar sky scans. This  
significantly reduces the number of valid SSA data points, making it unfeasible to characterize continuous intra-day variations.  
Similarly, such high-frequency analysis is also not available at the SGP site for either parameter.

We continue to explore the averaged diurnal cycles of AOD and SSA retrieved by ASI. We select the Beijing\_PKU site using  
245 data from May 2017 to May 2018. This one-year period was selected to ensure complete seasonal coverage while maintaining  
sufficient sample size within each seasonal group. All matched data from the independent test set within this period were  
grouped by season — Spring (Mar–May), Summer (Jun–Aug), Autumn (Sep–Nov), and Winter (Dec–Feb) — and the hourly  
mean and standard deviation of both AERONET observations and model retrievals were calculated within each seasonal group.  
All timestamps were converted from UTC to Beijing Local Standard Time (LST, UTC+8) prior to analysis. It should be noted  
250 that the diurnal coverage is confined to approximately 12:00–18:00 LST, corresponding to the period of direct solar  
illumination required for valid AERONET almucantar sky scan retrievals, which limits the representativeness of the full  
diurnal cycle but still captures the afternoon period.



255 **Figure 7: Averaged diurnal cycles of AOD at 440 nm at the Beijing\_PKU site, stratified by season: (a) Spring (Mar–May), (b) Summer (Jun–Aug), (c) Autumn (Sep–Nov), and (d) Winter (Dec–Feb). Black solid lines and gray shading represent the AERONET observed hourly means and  $\pm 1$  standard deviation, respectively. Colored dashed lines and shading indicate the means and variability of the corresponding model retrieval results. The diurnal coverage is limited to afternoon hours due to the temporal overlap between ASI acquisition and AERONET measurement windows.**

260 Figure 7 presents the averaged diurnal cycles of AOD at 440 nm at the Beijing\_PKU site across four seasons (12:00–18:00 LST). The seasonal contrast in AOD magnitude is pronounced, with summer exhibiting the highest loading ( $\sim 0.7$ – $0.8$ ) and winter the lowest ( $\sim 0.3$ ). The model retrievals successfully track the observed afternoon trends across all seasons, with the uncertainty ranges of observations and model overlapping in most cases. Winter shows the best agreement, while summer shows a slight underestimation around 16:00 LST. In autumn, both observations and model show a pronounced peak around 14:00 LST with large uncertainty bands, suggesting that this feature is driven by episodic pollution events rather than a

265 consistent diurnal pattern.

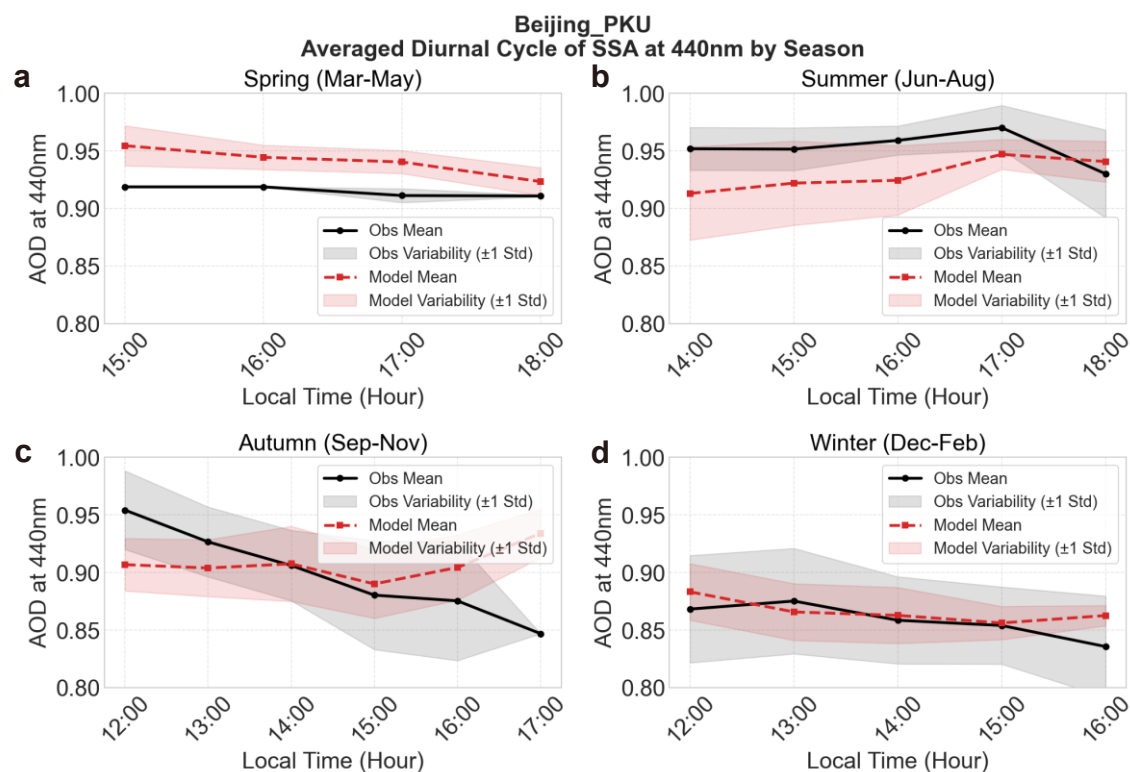
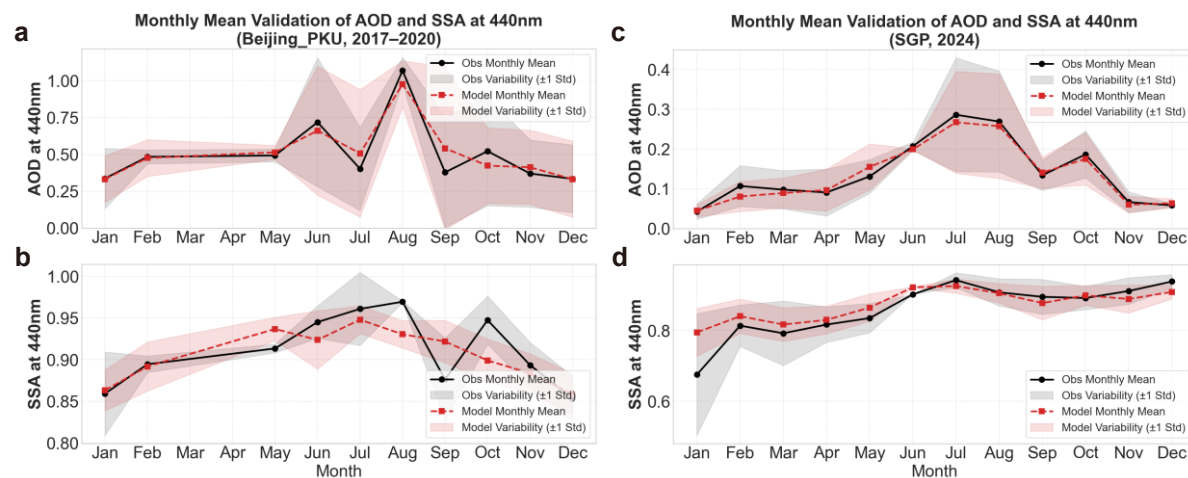


**Figure 8: Same as Figure 7 but for SSA at 440 nm.**

Figure 8 shows the corresponding diurnal cycles of SSA at 440 nm. SSA exhibits smaller diurnal variation compared to AOD across all seasons. In spring, the model systematically overestimates SSA by approximately 0.03, indicating a tendency to underestimate aerosol absorption. Summer shows similar underestimation behavior in the early afternoon. Winter performance is the best among all seasons, with the model mean closely tracking observations throughout the afternoon. Autumn shows the largest retrieval uncertainty and a diverging trend between observations and model after 15:00 LST, though the wide uncertainty bands suggest this may partly reflect high day-to-day variability rather than a systematic model bias.

### 3.4 Evaluation of Seasonal Variability

While Section 3.3 focuses on daily scale consistency, the following section further examines the temporal stability of the retrievals at seasonal scales for the Beijing and SGP sites, respectively.



280 **Figure 9: Monthly mean validation of AOD (upper panels) and SSA (lower panels) at 440 nm at the Beijing\_PKU site (a, b) and the SGP site (c, d). Black solid lines and gray shading denote the monthly means and  $\pm 1$  standard deviation of AERONET observations, respectively. Red dashed lines and pink shading represent the corresponding model retrieval means and variability. The standard deviation reflects the variability of all matched observations within each month across the full study period (Beijing: 2017–2020; SGP: 2024).**

Figure 9 presents the monthly mean validation of AOD and SSA at 440 nm for both the Beijing\_PKU and SGP sites. Overall, the model successfully reproduces the seasonal cycles of both parameters at both sites, with the modeled monthly means generally tracking the observed values throughout the year.

For AOD at the Beijing site (Fig. 9a), the seasonal cycle is well captured, with summer months (June–August) exhibiting the highest aerosol loading ( $\sim 0.7$ – $1.05$ ) and winter months the lowest ( $\sim 0.35$ ). The model agrees well with observations from January to May, while an underestimation is evident during the summer peak, particularly in August. A notable discrepancy also occurs in September, where the observed AOD drops sharply to  $\sim 0.38$  but the model retrieval remains at  $\sim 0.55$ , suggesting limited sensitivity to rapid aerosol loading transitions during the summer-to-autumn transition. For SSA at Beijing (Fig. 9b), the model tracks the observed seasonal variation reasonably well from January to May. However, a systematic underestimation of approximately  $0.03$ – $0.04$  is observed during summer (June–August), and the model fails to capture the sharp SSA decrease in September. The autumn months thus represent the most challenging period for SSA retrieval at this site.

At the SGP site, both AOD and SSA show good seasonal consistency between model and observations for most of the year. For AOD (Fig. 9c), the model closely follows the observed seasonal peak in summer and the low values in winter, with only a slight underestimation of  $0.02$ – $0.05$  during January–April. It is worth noting that June exhibits negligible variability in both observations and model retrievals (indicated by the near-absent shading), which is attributable to the extremely limited number of valid matched samples in that month — with only a single observation day available — rather than reflecting genuinely low aerosol variability. This should be considered when interpreting the June monthly mean. For SSA (Fig. 9d), the model performs well from June to December, with the two lines nearly overlapping and the uncertainty ranges mutually covering each other.



However, a notable overestimation is observed in January, where the model predicts  $\sim 0.80$  while the observed SSA is only  $\sim 0.68$ .

The consistency between retrieved and observed monthly means demonstrates that the proposed method is not sensitive to site-specific sampling density and exhibits good transferability across different climatic and geographical environments.

#### 305 4. Summary and Outlook

This study successfully constructed an XGBoost regression model based on visible-band image features from an All-Sky Imager and AERONET ground-based measurements, enabling the simultaneous joint retrieval of AOD and SSA across four spectral channels (440, 675, 870, 1020 nm). This approach replaces the iterative computation of traditional physical models with a data-driven, nonlinear mapping between sky radiance features and aerosol optical parameters, addressing a research gap in multi-dimensional aerosol parameter retrieval from ASIs.

The model demonstrated high reliability across all spectral bands. AOD retrievals showed the best performance, with Pearson correlation coefficients ( $r$ ) exceeding 0.86 across all wavelengths at both sites, RMSE ranging from 0.02 to 0.25, and mean absolute errors (MAE) below 0.15. SSA retrievals exhibited moderate but wavelength- and site-dependent performance: at the Beijing\_PKU site,  $r$  decreased from 0.67 at 440 nm to 0.33 at 1020 nm, while at the SGP site,  $r$  increased from 0.64 at 440 nm to 0.84 at 1020 nm. RMSE for SSA remained consistently low ( $\leq 0.09$ ) across all bands and both sites, confirming that the model correctly estimates SSA magnitudes within a reasonable margin of error despite the varying correlation performance.

Previous ASI-based retrieval studies have demonstrated promising AOD accuracy, with correlation coefficients exceeding 0.92 and MAE below 0.005 using machine learning approaches, or  $r^2$  of approximately 0.87 using radiative transfer inversion with the GRASP code. However, these methods are either restricted to AOD and Angström exponent retrieval, or rely on computationally intensive radiative transfer iterations, and none has demonstrated simultaneous SSA retrieval. Compared to traditional radiative transfer model iteration methods, the method achieves comparable AOD accuracy ( $r > 0.86$ , RMSE  $< 0.05$  at the SGP site) while simultaneously retrieving SSA for the first time using ASI imagery, representing a promising extension of ASI-based aerosol remote sensing capabilities. Furthermore, the data-driven XGBoost framework significantly reduces computational overhead compared to iterative radiative transfer approaches, making it well-suited to the high temporal resolution of all-sky imagers. Leveraging the instrument's low cost and ease of maintenance, it facilitates the establishment of high-density observation networks in regions lacking atmospheric stations, such as deserts and fields. This effectively helps bridge the observational gap arising from the low resolution of satellites and the sparse distribution of ground stations.

This study holds both theoretical and practical significance. On a theoretical level, the all-sky image feature-to-multi-optical-parameter mapping model established in this work enriches the machine learning application paradigm in aerosol remote sensing and provides methodological references for inversion studies integrating multi-source data. On a practical level, the approach can be directly applied in scenarios such as solar power plants and remote ecological reserves: high spatiotemporal resolution coordinated observations of AOD and SSA can be used to assess the impact of aerosols on surface solar radiation.



335 Meanwhile, this study has two main aspects open for improvement. First, the data coverage does not include samples from extreme environments such as high-latitude regions and deserts, thus the global generalizability of the conclusions requires further validation. Second, the lack of integrated aerosol vertical distribution information prevents the distinction of parameter differences between the boundary layer and the free atmosphere. In the future, we will continue to explore the applicability of ASI in retrieving different aerosol parameters as well as under different environments.

### Data Availability Statement

340 The datasets used and analyzed during the current study are available from various sources. The all-sky imager (ASI) data collected at the Beijing\_PKU site are proprietary to our research group and are available from the corresponding author upon reasonable request. The ASI images for the Southern Great Plains (SGP) site are publicly available through the Atmospheric Radiation Measurement (ARM) user facility data archive (<https://adc.arm.gov/discovery/>). Additionally, the reference aerosol optical parameters can be accessed via the Aerosol Robotic Network (AERONET) database (<https://aeronet.gsfc.nasa.gov/>).

### Author contributions

345 J.L. conceptualized the research, and provided overall supervision. H.N. was responsible for the research design, performing the experiments, data collection and processing, and drafting the manuscript. Z.Z. provided the essential data for the study. L.C., Y.D., G.D., M.L., Q.L., G.L., Y.S., A.T., S.Y. and C.Z. contributed to the maintenance and management of the instruments. J.L. and H.N. performed the data analysis and results discussion, contributed to the critical revision of the manuscript and approved the final version.

### 350 Competing interests

The authors declare that a patent application related to the method described in this manuscript has been filed by Peking University (Application No. CN202511448418.3). The authors have no other competing interests.

### Acknowledgements

355 This study is funded by the National Natural Science Foundation of China (Grant No. 42425503 and 42375121) and the Beijing Natural Science Foundation (Grant No. QY25158).



## References

- Anon: Picture Thresholding Using an Iterative Selection Method, *IEEE Trans. Syst., Man, Cybern.*, 8, 630–632, <https://doi.org/10.1109/TSMC.1978.4310039>, 1978.
- Arlot, S. and Celisse, A.: A Survey of Cross Validation Procedures for Model Selection, *Statistics Surveys*, 4,   
360 <https://doi.org/10.1214/09-SS054>, 2009.
- Bellouin, N., Quaas, J., Gryspeerdt, E., Kinne, S., Stier, P., Watson-Parris, D., Boucher, O., Carslaw, K. S., Christensen, M., Daniau, A.-L., Dufresne, J.-L., Feingold, G., Fiedler, S., Forster, P., Gettelman, A., Haywood, J. M., Lohmann, U., Malavelle, F., Mauritsen, T., McCoy, D. T., Myhre, G., Mülmenstädt, J., Neubauer, D., Possner, A., Rugenstein, M., Sato, Y., Schulz, M., Schwartz, S. E., Sourdeval, O., Storelvmo, T., Toll, V., Winker, D., and Stevens, B.: Bounding Global Aerosol Radiative Forcing of Climate Change, *Reviews of Geophysics*, 58, e2019RG000660, <https://doi.org/10.1029/2019RG000660>, 2020.   
365
- Boucher, O., Randall, D., Artaxo, P., Bretherton, C., Feingold, G., Forster, P., Kerminen, V.-M., Kondo, Y., Liao, H., Lohmann, U., Rasch, P., Satheesh, S., Sherwood, S., Stevens, B., and Zhang, X.: *Clouds and Aerosols*, 571–892, 2013.
- Cazorla, A., Shields, J. E., Karr, M. E., Olmo, F. J., Burden, A., and Alados-Arboledas, L.: Technical Note: Determination of aerosol optical properties by a calibrated sky imager, *Atmos. Chem. Phys.*, 9, 6417–6427, <https://doi.org/10.5194/acp-9-6417-2009>, 2009.   
370
- Chai, T. and Draxler, R. R.: Root mean square error (RMSE) or mean absolute error (MAE)? – Arguments against avoiding RMSE in the literature, *Geoscientific Model Development*, 7, 1247–1250, <https://doi.org/10.5194/gmd-7-1247-2014>, 2014.
- Chen, T. and Guestrin, C.: XGBoost: A Scalable Tree Boosting System, in: *Proceedings of the 22nd ACM SIGKDD International Conference on Knowledge Discovery and Data Mining, KDD '16: The 22nd ACM SIGKDD International Conference on Knowledge Discovery and Data Mining*, 785–794, <https://doi.org/10.1145/2939672.2939785>, 2016.   
375
- Cook, D. and Sullivan, R.: *Energy Balance Bowen Ratio (EBBR) Instrument Handbook*, 2025.
- Dubovik, O. and King, M. D.: A flexible inversion algorithm for retrieval of aerosol optical properties from Sun and sky radiance measurements, *J. Geophys. Res.*, 105, 20673–20696, <https://doi.org/10.1029/2000JD900282>, 2000.
- Dubovik, O., Smirnov, A., Holben, B., King, M., Kaufman, Y. J., Eck, T., and Slutsker, I.: Accuracy assessment of aerosol optical properties retrieved from Aerosol Robotic Network (AERONET) Sun and sky radiance measurements, *Journal of Geophysical Research*, 105, 9791–9806, <https://doi.org/10.1029/2000JD900040>, 2000.   
380
- García, R. D., Barreto, Á., Rey, C., Fraile-Nuez, E., González-Vega, A., León-Luis, S. F., Alcántara, A., Almansa, A. F., Guirado-Fuentes, C., González-Sicilia, P., Cachorro, V. E., and Bouchard, F.: Aerosol retrievals derived from a low-cost Calitoo sun-photometer taken on board a research vessel, *Atmospheric Environment*, 341, 120888, <https://doi.org/10.1016/j.atmosenv.2024.120888>, 2025.   
385
- Ghonima, M. S., Urquhart, B., Chow, C. W., Shields, J. E., Cazorla, A., and Kleissl, J.: A method for cloud detection and opacity classification based on ground based sky imagery, *Atmos. Meas. Tech.*, 5, 2881–2892, <https://doi.org/10.5194/amt-5-2881-2012>, 2012.
- Gonzalez, R. and Faisal, Z.: *Digital Image Processing Second Edition*, 2019.
- Hansen, J., Sato, M., and Ruedy, R.: Radiative forcing and climate response, *Journal of Geophysical Research: Atmospheres*, 102, 6831–6864, <https://doi.org/10.1029/96JD03436>, 1997.   
390



- Hao, H., Wang, K., Zhao, C., Wu, G., and Li, J.: Visibility-derived aerosol optical depth over global land from 1959 to 2021, *Earth System Science Data*, 16, 3233–3260, <https://doi.org/10.5194/essd-16-3233-2024>, 2024.
- 395 Holben, B. N., Eck, T. F., Slutsker, I., Tanré, D., Buis, J. P., Setzer, A., Vermote, E., Reagan, J. A., Kaufman, Y. J., Nakajima, T., Lavenu, F., Jankowiak, I., and Smirnov, A.: AERONET—A Federated Instrument Network and Data Archive for Aerosol Characterization, *Remote Sensing of Environment*, 66, 1–16, [https://doi.org/10.1016/S0034-4257\(98\)00031-5](https://doi.org/10.1016/S0034-4257(98)00031-5), 1998.
- Huo, J. and Lü, D.: Preliminary retrieval of aerosol optical depth from all-sky images, *Advances in Atmospheric Sciences*, 27, 421–426, <https://doi.org/10.1007/s00376-009-8216-2>, 2010.
- 400 Intergovernmental Panel On Climate Change (Ipcc): *Climate Change 2021 – The Physical Science Basis: Working Group I Contribution to the Sixth Assessment Report of the Intergovernmental Panel on Climate Change*, 1st ed., Cambridge University Press, <https://doi.org/10.1017/9781009157896>, 2023.
- Jenkins, D. and Quintana-Ascencio, P.: A solution to minimum sample size for regressions, *PLOS ONE*, 15, e0229345, <https://doi.org/10.1371/journal.pone.0229345>, 2020.
- 405 Karpatne, A., Ebert-Uphoff, I., Ravela, S., Babaie, H., and Kumar, V.: Machine Learning for the Geosciences: Challenges and Opportunities, *IEEE Transactions on Knowledge and Data Engineering (in review)*, 31, <https://doi.org/10.1109/TKDE.2018.2861006>, 2017.
- Kazantzidis, A., Tzoumanikas, P., Bais, A. F., Fotopoulos, S., and Economou, G.: Cloud detection and classification with the use of whole-sky ground-based images, *Atmospheric Research*, 113, 80–88, <https://doi.org/10.1016/j.atmosres.2012.05.005>, 2012.
- 410 Kazantzidis, A., Tzoumanikas, P., Nikitidou, E., Salamalikis, V., Wilbert, S., and Prah, C.: Application of simple all-sky imagers for the estimation of aerosol optical depth, *SOLARPACES 2016: International Conference on Concentrating Solar Power and Chemical Energy Systems*, 140012, <https://doi.org/10.1063/1.4984520>, 2017.
- Lary, D. J., Alavi, A. H., Gandomi, A. H., and Walker, A. L.: Machine learning in geosciences and remote sensing, *Geoscience Frontiers*, 7, 3–10, <https://doi.org/10.1016/j.gsf.2015.07.003>, 2016.
- 415 Legates, D. R. and McCabe Jr., G. J.: Evaluating the use of “goodness-of-fit” Measures in hydrologic and hydroclimatic model validation, *Water Resources Research*, 35, 233–241, <https://doi.org/10.1029/1998WR900018>, 1999.
- Levy, R. C., Mattoo, S., Munchak, L. A., Remer, L. A., Sayer, A. M., Patadia, F., and Hsu, N. C.: The Collection 6 MODIS aerosol products over land and ocean, *Atmospheric Measurement Techniques*, 6, 2989–3034, <https://doi.org/10.5194/amt-6-2989-2013>, 2013.
- 420 Li, Z., Guo, J., Ding, A., Liao, H., Liu, J., Sun, Y., Wang, T., Xue, H., Zhang, H., and Zhu, B.: Aerosol and boundary-layer interactions and impact on air quality, *National Science Review*, 4, 810–833, <https://doi.org/10.1093/nsr/nwx117>, 2017.
- Logothetis, S.-A., Giannaklis, C.-P., Salamalikis, V., Tzoumanikas, P., Raptis, P., Amiridis, V., Eleftheratos, K., and Kazantzidis, A.: Aerosol Optical Properties and Type Retrieval via Machine Learning and an All-Sky Imager, *Atmosphere*, 14, 1266, <https://doi.org/10.3390/atmos14081266>, 2023a.
- 425 Logothetis, S.-A., Giannaklis, C.-P., Salamalikis, V., Tzoumanikas, P., Raptis, P.-I., Amiridis, V., Eleftheratos, K., and Kazantzidis, A.: Retrieval of Aerosol Optical Properties via an All-Sky Imager and Machine Learning: Uncertainty in Direct Normal Irradiance Estimations, <https://doi.org/10.3390/envirosci2023026133>, 2023b.



- 430 Logothetis, S.-A., Giannaklis, C.-P., Salamalikis, V., Tzoumanikas, P., Raptis, P.-I., Amiridis, V., Eleftheratos, K., and Kazantzidis, A.: Retrieval of Aerosol Optical Properties via an All-Sky Imager and Machine Learning: Uncertainty in Direct Normal Irradiance Estimations, <https://doi.org/10.3390/envirosci2023026133>, 2023c.
- Long, C. N., Sabburg, J. M., Calbó, J., and Pagès, D.: Retrieving Cloud Characteristics from Ground-Based Daytime Color All-Sky Images, *Journal of Atmospheric and Oceanic Technology*, 23, 633–652, <https://doi.org/10.1175/JTECH1875.1>, 2006.
- Olmo, F., Cazorla, A., Arboledas, L., López-Álvarez, M., Hernández-Andrés, J., and Romero, J.: Retrieval of the optical depth using an all-sky CCD camera, *Applied Optics*, 47, H182–H189, <https://doi.org/10.1364/AO.47.00H182>, 2008.
- 435 Roberts, D. R., Bahn, V., Ciuti, S., Boyce, M. S., Elith, J., Guillera-Arroita, G., Hauenstein, S., Lahoz-Monfort, J. J., Schröder, B., Thuiller, W., Warton, D. I., Wintle, B. A., Hartig, F., and Dormann, C. F.: Cross-validation strategies for data with temporal, spatial, hierarchical, or phylogenetic structure, *Ecography*, 40, 913–929, <https://doi.org/10.1111/ecog.02881>, 2017.
- Román, R., Antuña-Sánchez, J. C., Cachorro, V. E., Toledano, C., Torres, B., Mateos, D., Fuertes, D., López, C., González, R., Lapionok, T., Herreras-Giralda, M., Dubovik, O., and de Frutos, Á. M.: Retrieval of aerosol properties using relative radiance measurements from an all-sky camera, *Atmospheric Measurement Techniques*, 15, 407–433, <https://doi.org/10.5194/amt-15-407-2022>, 2022.
- 440 Rossini, E. G. and Krenzinger, A.: Maps of sky relative radiance and luminance distributions acquired with a monochromatic CCD camera, *Solar Energy*, 81, 1323–1332, <https://doi.org/10.1016/j.solener.2007.06.013>, 2007.
- Sabburg, J. and Wong, J.: Evaluation of a Ground-Based Sky Camera System for Use in Surface Irradiance Measurement, *J. Atmos. Oceanic Technol.*, 16, 752–759, [https://doi.org/10.1175/1520-0426\(1999\)016%3C0752:EOAGBS%3E2.0.CO;2](https://doi.org/10.1175/1520-0426(1999)016%3C0752:EOAGBS%3E2.0.CO;2), 1999.
- 445 Scarlatti, F., Gómez-Amo, J., C. Valdelomar, P., Estellés, V., and Utrillas, M.: A Machine Learning Approach to Derive Aerosol Properties from All-Sky Camera Imagery, *Remote Sensing*, 15, <https://doi.org/10.3390/rs15061676>, 2023.
- Snik, F., Rietjens, J. H. H., Apituley, A., Volten, H., Mijling, B., Di Noia, A., Heikamp, S., Heinsbroek, R. C., Hasekamp, O. P., Smit, J. M., Vonk, J., Stam, D. M., van Harten, G., de Boer, J., Keller, C. U., and Scientists, 3187 iSPEX citizen: Mapping atmospheric aerosols with a citizen science network of smartphone spectropolarimeters, *Geophysical Research Letters*, 41, 7351–7358, <https://doi.org/10.1002/2014GL061462>, 2014.
- 450 Stokes, G. M. and Schwartz, S. E.: The Atmospheric Radiation Measurement (ARM) Program: Programmatic Background and Design of the Cloud and Radiation Test Bed, *Bulletin of the American Meteorological Society*, 75, 1201–1222, [https://doi.org/10.1175/1520-0477\(1994\)075%3C1201:TARMPP%3E2.0.CO;2](https://doi.org/10.1175/1520-0477(1994)075%3C1201:TARMPP%3E2.0.CO;2), 1994.
- Tohsing, K., Schrempf, M., Riechelmann, S., and Seckmeyer, G.: Validation of spectral sky radiance derived from all-sky camera images - A case study, *Atmospheric Measurement Techniques*, 7, <https://doi.org/10.5194/amt-7-69-2014>, 2013.
- 460 Valdelomar, P., Gómez-Amo, J. L., Peris-Ferrús, C., Scarlatti, F., and Utrillas, M. P.: Feasibility of Ground-Based Sky-Camera HDR Imagery to Determine Solar Irradiance and Sky Radiance over Different Geometries and Sky Conditions, *Remote Sensing*, 13, 5157, <https://doi.org/10.3390/rs13245157>, 2021.
- Zhang, Q. and Xiao, C.: Cloud Detection of RGB Color Aerial Photographs by Progressive Refinement Scheme, *Geoscience and Remote Sensing, IEEE Transactions on*, 52, 7264–7275, <https://doi.org/10.1109/TGRS.2014.2310240>, 2014.